Available online at www.keaipublishing.com/en/journals/journal-of-magnesium-and-alloys/

ScienceDirect

Journal of Magnesium and Alloys 13 (2025) 3918–3930

www.elsevier.com/locate/jma

Full Length Article

# In vitro and in vivo degradation behavior of a corrosion-resistant Mg alloy with combined addition of rare-earth elements[☆]

Du-Won Min[a], Young Hee Kim[b], Jaeho Kwon[a], Jeong-Ki Kim[a], Cholong Choi[a], Eunhye Yun[a], Chaenyung Cha[a], Seong Hoon Choi[c], Hojong Park[d], Jung Gu Lee[e], Byungsuk Kwon[b], Sang Jun Park[d,*], Sung Soo Park[a,*]

[a] Department of Materials Science and Engineering, Ulsan National Institute of Science and Technology, Ulsan 44919, Republic of Korea
[b] School of Biological Sciences, University of Ulsan, Ulsan 44610, Republic of Korea
[c] Department of Radiology, Ulsan University Hospital and University of Ulsan College of Medicine, Ulsan 44033, Republic of Korea
[d] Department of Surgery, Ulsan University Hospital and University of Ulsan College of Medicine, Ulsan 44033, Republic of Korea
[e] School of Materials Science and Engineering, University of Ulsan, Ulsan 44776, Republic of Korea

Received 29 April 2025; received in revised form 24 June 2025; accepted 11 July 2025
Available online 19 August 2025

## Abstract

The in vitro and in vivo degradation behavior of an experimental Mg alloy with high corrosion resistance has been investigated and compared with that of a commercial AZ31 Mg alloy with a similar chemical composition. In vitro tests indicated that the experimental alloy is >2.5 times more resistant to degradation than AZ31 during immersion in HBSS at 37 °C for 72 h. In vivo tests in the femoral vein of a mouse confirmed that the former degrades much more slowly and uniformly in the biological environment than the latter. Compared with WE43 and JDBM alloys, which are currently considered promising candidates for Mg-based biodegradable materials, the experimental alloy in this study showed better degradation resistance with a similar level of biocompatibility. Microstructural and electrochemical factors affecting the degradation behavior of the alloys in this study are also discussed.

*Keywords:* Magnesium alloy; Corrosion resistance; Microstructure; Degradation; Biocompatibility.

## 1. Introduction

Non-biodegradable implants, typically based on stainless steels, Ti alloys, or Co–Cr alloys, can cause various side effects after implantation in the human body [1–3]. This is considered even more serious for stent-type implants, which cannot be easily removed by secondary surgery after recovery. In the case of a cardiovascular stent, the foreign body reaction between the permanent stent material and the surrounding tissue can cause restenosis and thrombosis [4–10]. In light of this, research has been actively conducted to develop biodegradable metal implants, which inherently do not have to be removed via secondary surgery.

Among various metallic elements, readily corrodible elements such as Mg, Fe, and Zn are candidate materials for biodegradable implants [11–18]. Mg is regarded as one of the most feasible materials for this purpose since it can be easily excreted in the urine after degradation in the body [2,14,19–22]. In addition, Mg-based alloy materials have higher strength compared to biodegradable polymers and are free from ferromagnetism-induced interference in the body during MRI examination [23]. However, conventional commercial Mg alloys, such as Mg–3Al–1Zn–0.3Mn (AZ31) (wt.%), generally undergo rapid and localized degradation in aqueous environments containing salt such as seawater or blood, resulting in premature decay after implantation [24–30]. Furthermore, $H_2$ gas bubbles generated during Mg degra-

---

[☆] Peer review under the responsibility of Chongqing University
[*] Corresponding authors.
*E-mail addresses:* sjpark@uuh.ulsan.kr (S.J. Park), sspark@unist.ac.kr (S.S. Park).

https://doi.org/10.1016/j.jma.2025.07.007

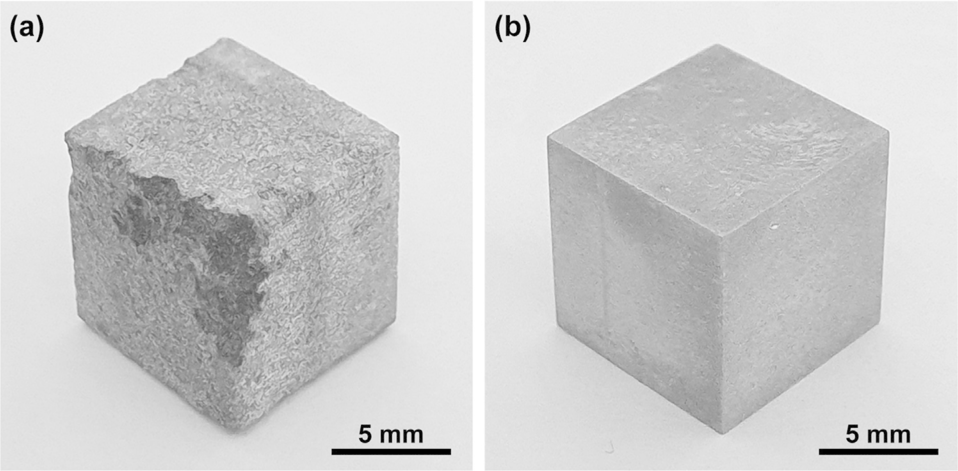

Fig. 1. Optical micrographs of the (a) AZ31 and (b) AZ31-GS alloys in the cast condition after immersion in 0.6 M NaCl solution at 25 °C for two weeks.

Table 1
Analyzed compositions (wt.%) of the Mg alloys investigated in this study.

| Alloy | Al | Zn | Mn | Gd | Sc | Fe | Si | Mg |
|---|---|---|---|---|---|---|---|---|
| AZ31 | 3.15 | 1.02 | 0.346 | <0.001 | <0.001 | 0.0051 | 0.0244 | Bal. |
| AZ31-GS | 3.12 | 1.00 | 0.330 | 0.281 | 0.091 | 0.0041 | 0.0251 | Bal. |

dation can cause inflammation by creating cavities in the tissue [26,27,31,32].

Recent reports on stent-type Mg-based implants indicated that a Mg–Nd–Zn–Zr alloy for a JDBM stent maintained its structure and properties during in vivo implantation for roughly six months [1]. WE43-based alloys for the BIOTRONIK AMS stent were implanted into the coronary artery of a patient and showed stability for approximately four months [33]. Despite such prolonged degradation periods, these Mg alloys still provide insufficient degradation resistance in their bare metal condition [34,35]. In particular, non-uniform degradation behavior that occurs in the absence of a surface coating layer during long-term clinical trials is the most critical disadvantage of the existing biodegradable Mg alloy stents [35,36]. As an alternative to the current Mg alloy candidates for biodegradable applications, the authors propose an experimental Mg alloy with enhanced degradation resistance with a nominal composition of Mg–3Al–1Zn–0.3Mn–0.3Gd–0.1Sc (AZ31-GS) in wt.%. This alloy incorporates primary intermetallic particles containing two rare-earth (RE) elements that can capture noble impurity elements such as Fe to effectively suppress microgalvanic corrosion caused by impurities in the conventional Mg–Al–Zn–Mn-based alloy system. Depending on the ratios of Gd to Sc added to this experimental alloy, the formation temperature and volume fraction of the primary particles can change.

The new type of Mg alloy with RE micro-addition has a ten times slower corrosion rate than that of a commercial AZ31 alloy in a typical saline solution. As presented in Fig. 1, average corrosion rates based on weight-loss obtained after immersion in a 0.6 M NaCl solution at 25 °C for two weeks were 1.9 and 0.18 mm year$^{-1}$ for the AZ31 and AZ31-GS alloys, respectively. In terms of the content of major alloying elements, the AZ31-GS alloy can be considered a highly corrosion-resistant version of AZ31 alloy, which is a representative Mg alloy having balanced mechanical properties appropriate for biodegradable stent applications. It should be noted that neurotoxicity in biological environments is a possible concern for Mg alloys containing Al. However, a cardiovascular stent made from commercial AZ31 alloy leaches <1 % of the Temporary Tolerable Weekly Intake (PTWI) of Al proposed by the FAO/WHO Expert Committee on Food Additives (JECFA) [37,38], and the highly corrosion-resistant AZ31-GS alloy is expected to leach even smaller amounts of Al into the human body than its commercial counterpart. In this study, based on the corrosion-proof performance of the experimental alloy in a saline solution, the in vitro and in vivo degradation behaviors and biocompatibility of the experimental and conventional Mg alloys were comparatively investigated to explore the possibility of employing the new type of Mg alloy in future biodegradable implant applications.

## 2. Experimental

### 2.1. Sample preparation and microstructural characterization

The analyzed chemical compositions of the AZ31 and AZ31-GS alloys are provided in Table 1. Alloys were prepared by induction melting with purging of a $CO_2$ and $SF_6$ mixture. During casting, molten metal was held at 750 °C for 15 min and then poured into a steel mold pre-heated to 200 °C. The cast samples are 12 mm in thickness, 50 mm in width, and 100 mm in height. To prepare thin sheets for in vitro and in vivo degradation tests, the rectangular cast samples were heat-treated at 420 °C for one hour, followed by water quenching, and then hot-rolled at 350 °C to prepare sheets. The rolling process was repeated with a thickness reduction ratio of 20 % per pass until the final thickness reached 1.1 mm. This thin-gauged sheet was finally annealed at 345 °C for one hour.

Samples for microstructural characterization were prepared by mechanical grinding and surface polishing. Mechanical grinding was carried out in a water atmosphere with SiC papers up to 1200 grit. Surface polishing was performed in an ethanol atmosphere with 1.0 $\mu$m diamond paste and a 0.04 $\mu$m colloidal silica solution. Microstructural investigations were performed with a Keyence VHX-6000 optical microscope (OM), a FEI Quanta 200 field-emission scanning electron microscope (SEM), an EDAX Apollo X energy-dispersive spectrometer (EDS), and a Tecnai 2 G F20 X-Twin transmission electron microscope (TEM). Samples for the TEM analysis were prepared with Quanta 3D FEG focused ion beam equipment. The Volta potential difference between the $\alpha$-Mg matrix and intermetallic phases in the alloys was measured by scanning Kelvin probe force microscopy (SKPFM). All SKPFM measurements were performed in atmospheric conditions at room temperature with a Bruker Dimension ICON atomic force microscope and the sample preparation method for SKPFM corresponded with that used for the OM and SEM analyses. X-ray diffraction (XRD) analysis was conducted with a Rigaku D/MAX-2500/PC in back reflection mode with Cu-$K_\alpha$ radiation.

### 2.2. In vitro degradation tests and electrochemical analysis

In vitro tests were conducted by immersing sheet-type samples ($10 \times 10 \times 1$ mm$^3$) in deaerated Hanks' Balanced Salt Solution (HBSS) at 37 °C for up to 72 h. The surface condition of the samples was the same as that for the microstructural characterization. To exactly measure weight loss during immersion in HBSS, surficial oxide products formed by degradation were cleaned using a solution consisting of 200 g L$^{-1}$ $CrO_3$, 10 g L$^{-1}$ $AgNO_3$, and 20 g L$^{-1}$ $Ba(NO_3)_2$ at 25 °C. Statistical analysis was conducted to evaluate the difference in degradation rates between the alloys. A two-tailed p-value was calculated using an unpaired *t*-test with three samples for each alloy. A Gamry Reference 600 potentiostat was used for potentiodynamic polarization tests and electrochemical impedance spectroscopy (EIS) measurements after immersing the alloy samples in HBSS at 37 °C for one hour before any local damage to the oxide layer occurred. A conventional three-electrode cell composed of a working electrode (sample), a saturated calomel reference electrode (SCE), and a Pt plate counter electrode was used. During polarization tests, the exposed area of the sample was 0.1256 cm$^2$ and the potential sweep rate was 1 mV s$^{-1}$. EIS measurements were performed with AC perturbation amplitude of 10 mV over a scanning frequency range of 100 kHz to 10 mHz for the Nyquist plots.

### 2.3. In vivo degradation tests

In vivo tests were conducted with C57BL/6 (male, 10-week-old) mice supplied by KOATECH, Korea. The tests were approved by the Animal Care Committee of the University of Ulsan. The mice were anesthetized by intramuscular injection and an incision was made in the skin on the side of one leg to expose the femoral vein. The leg side of the femoral vein was tied to block blood flow while the implantation was in progress, and a wire-shaped alloy sample was implanted after the outer wall of the blood vessel was scratched. The incised skin was sutured and the mice were left on a heating pad while under anesthesia. The alloy samples for in vivo testing were prepared by cutting and grinding the hot-rolled sheet to produce thin cone-shaped wires with diameters ranging from 0.35 to 0.45 mm to allow insertion into the blood vessel. The weight and health conditions of each mouse were checked weekly after implantation and there were no abrupt weight changes or visible side effects up to 12 weeks. The in vivo degradation behavior of the implanted Mg alloy samples was observed every week with a Bruker Skyscan 1176 micro-computed tomography (micro-CT) scanner. X-ray exposure with anesthesia time per shot was limited to $<10$ min. The mice were euthanized after 12 weeks and then the implanted samples were retrieved. The in vivo degradation rate of the retrieved wire samples was evaluated using the same method as employed for the in vitro weight loss tests. Three mice were provided per alloy wire sample.

### 2.4. Cell viability tests

Human umbilical vein endothelial cells (HUVECs) were used to evaluate the biocompatibility of the AZ31 and AZ31-GS alloys. Endothelial Cell Basal Medium-2 (EBM-2, LONZA) enriched with an EGM-2 Single QuotsTM kit (containing 1 % penicillin/streptomycin) provided supplements and growth factors required for HUVEC culture. The cell culture medium was changed every other day. To determine the cytotoxicity of the Mg alloy extract, in vitro cell viability tests were performed by Live/Dead cell staining and an MTT assay. The sheet-type alloy samples ($12.5 \times 12.5 \times 1$ mm$^3$) were immersed in 3 mL of a cell culture medium and then incubated at 37 °C in 5 % $CO_2$. The conditioned media with extracted Mg and alloying elements were collected after three days. Cells were seeded in each well of a 96-well plate with 20,000 cells/well density. After the cells were incubated overnight to fully cover the plate, the cell culture medium was replaced with a 50 % concentration of conditioned medium and cultured for another 24 h to confirm their cytotoxicity. For Live/Dead cell staining, the cell viability was evaluated by the percentage of live cells from the total cells after treating the conditioned medium. The live cells were fluorescently visualized with calcein-AM (green) and dead cells were labeled with ethidium homodimer-1 (red) (Thermo Fisher Scientific LIVE/DEAD® Viability/Cytotoxicity Assay kit). For the MTT assay, the cells were treated with 0.5 mg mL$^{-1}$ of 3-(4,5-dimethylthiazol-2-yl)-2,5-diphenyltetrazolium bromide (Sigma Aldrich MTT) in the culture medium for four hours at 37 °C in a 5 % $CO_2$. The MTT stop solution containing 20 % sodium dodecyl sulfate was then added in equal volume to MTT solution. The absorbance at 570 nm was measured to quantify reduced MTT by living cells. All

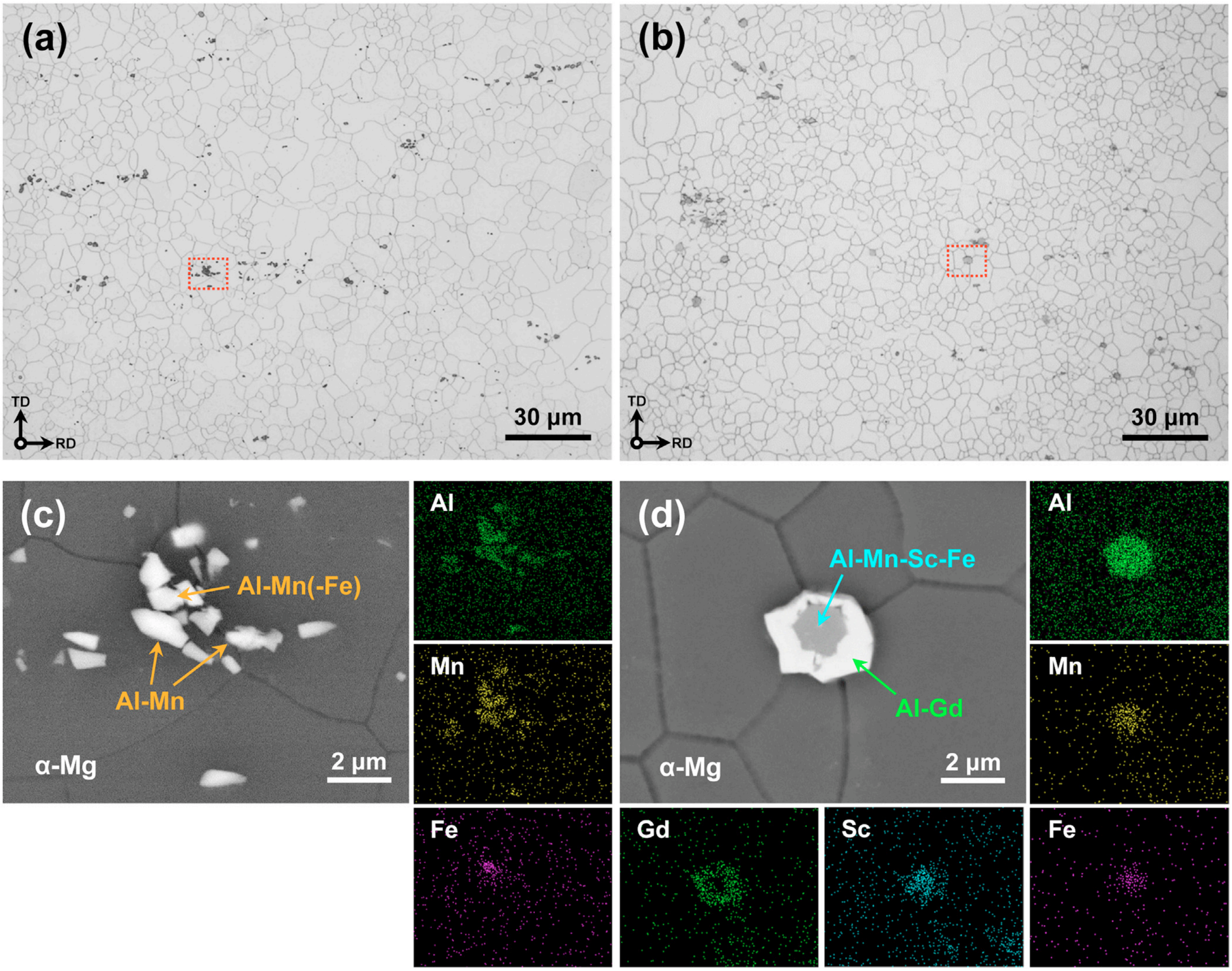

Fig. 2. Low-magnification optical micrographs of the (a) AZ31 and (b) AZ31-GS alloys in the hot-rolled condition and high-magnification SEM micrographs showing the major intermetallic particles observed in the low-magnification micrographs of the (c) AZ31 and (d) AZ31-GS alloys with corresponding EDS maps for the elements Al, Mn, and Fe in AZ31 and Al, Mn, Gd, Sc, and Fe in AZ31-GS.

measurements or tests performed in this study were performed three times to ensure reproducibility.

## 3. Results and discussion

### *3.1. Microstructure*

Fig. 2a and b present optical micrographs of the AZ31 and AZ31-GS alloys in the hot-rolled condition. The two alloys similarly show wrought microstructures consisting of fine $\alpha$-Mg grains and sparse second-phase particles. The average grain sizes of the AZ31 and AZ31-GS alloys measured 8.8 and 8.1 μm, respectively. These results indicate that the grain size of AZ31 was slightly refined by combined RE microalloying with Gd and Sc. More dramatic changes in the microstructure due to the RE microalloying occurred in the presence of second-phase particles. As shown in the SEM micrographs and corresponding EDS maps provided in Fig. 2c and d, the AZ31 alloy contains Al-Mn particles with different levels of Fe content, while these Al-Mn particles were not detectable and instead a core-shell type of particle was mainly observed in the AZ31-GS alloy. As indicated in the EDS maps, the core part is richer in Al, Mn, Sc, and Fe and the shell part has greater chemical intensity for Al and Gd than the $\alpha$-Mg matrix. This indicates that the core and shell parts consist of different types of crystal phase. Based on the TEM diffraction and EDS analysis results provided in Fig. 3, the particles present in AZ31 were determined to be body-centered cubic $Al_8Mn_5$ phase regardless of Fe content in the particles. From the analysis of the core-shell parts in AZ31-GS, the core part was identified as tetragonal $Al_8Mn_4Sc$ containing Fe and the shell part coincides with face-centered cubic $Al_2Gd$, thus confirming that the core and shell parts of the particle have different crystal structures. It should be noted here that the $Al_8Mn_4Sc$ phase with relatively high Fe intensity is completely encapsulated by the $Al_2Gd$ phase where Fe is not as concentrated. Detailed microstructural observations indicated that not all particles have a core-shell structure and

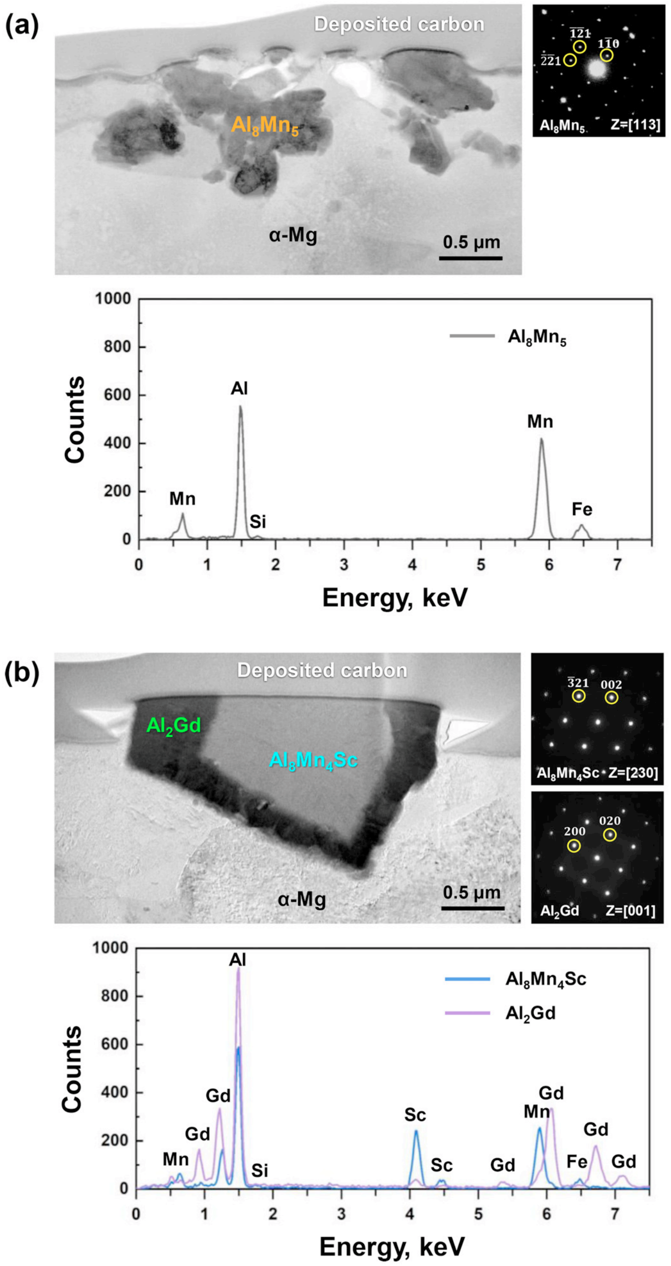

Fig. 3. TEM micrographs showing the major intermetallic particles in the hot-rolled (a) AZ31 and (b) AZ31-GS alloys with diffraction patterns and EDS spectra obtained from the particles.

that some $Al_8Mn_4Sc$ and $Al_2Gd$ phases with low Fe content exist separately in the AZ31-GS alloy. Image analysis indicated that the total volume fraction of these particles present in AZ31-GS is about 0.69 %, and the volume fraction of the core-shell structure particles (0.49% ± 0.06 %) is >70 % of the total.

### 3.2. SKPFM analysis

The above microstructural results indicate that the experimental AZ31-GS alloy is free from the well-known detrimental effect of Fe-rich $Al_8Mn_5$ particles on microgalvanic corrosion that is frequently observed in commercial AZ-series Mg alloys in corrosive environments [32,39–41]. Because the newly found $Al_8Mn_4Sc$ and $Al_2Gd$ phases could provide media for microgalvanic corrosion in AZ31-GS depending on their electrochemical nobility, Volta potential maps were acquired by SKPFM for both the AZ31 and AZ31-GS alloys, as provided in Fig. 4. Regardless of the phase types, the Volta potential of the particles containing Al was higher than that of the $\alpha$-Mg matrix. This indicates that the particles have a greater level of electrochemical nobility than the $\alpha$-Mg matrix and they can act as micro-cathodes in microgalvanic coupling with the $\alpha$-Mg. In more detail, the $Al_8Mn_5$ particles in AZ31 showed 300 $\sim$ 430 mV higher Volta potential values than the $\alpha$-Mg matrix depending on their Fe content. On the other hand, the Volta potential of the core and shell parts in AZ31-GS was measured to be about 290 and 100 mV higher, respectively, than that of the $\alpha$-Mg matrix. Since the Volta potential of a phase has been known to be closely related to the electrochemical properties of each element constituting the phase [42], it can be understood that $Al_2Gd$ with low Fe content and high RE content has the lowest Volta potential difference relative to the $\alpha$-Mg matrix. Note that the Volta potential of the shell part, which is in direct contact with the $\alpha$-Mg matrix in AZ31-GS, is about four times lower than that of the Fe-rich $Al_8Mn_5$ phase in AZ31. This suggests that the overall driving force for microgalvanic corrosion in AZ31-GS without the $Al_8Mn_5$ particles containing Fe would be much lower than that in AZ31.

### 3.3. In vitro degradation behavior in HBSS

Fig. 5 shows low-magnification optical micrographs of the AZ31 and AZ31-GS alloys after immersion in HBSS for 12–72 h. After immersion for 12 h, the AZ31 alloy exhibited severe filiform-like degradation while only a small part of the AZ31-GS alloy showed such behavior. While both the AZ31 and AZ31-GS alloys were more damaged after prolonged immersion for 72 h, the latter showed more uniform degradation behavior compared to the former. Based on the weight loss values after immersion in HBSS for 72 h, the AZ31 and AZ31-GS alloys exhibited degradation rates of 1.09 ± 0.15 and 0.40 ± 0.01 mm year$^{-1}$, respectively, indicating that the latter is >2.5 times more degradation-resistant than the former in the given in vitro conditions. This is supported by a difference in Al ion release during immersion; the released Al ion concentrations after immersion in HBSS for 72 h measured about 0.31 and 0.12 mg L$^{-1}$ for the AZ31 and AZ31-GS alloys, respectively. The statistical significance of this 2.5-fold improvement was also confirmed by a calculated p-value of $<0.0012$. It should be noted that the degradation rate of the AZ31-GS alloy in this study is lower than the degradation rate values found in the literature (0.5–1.9 mm year$^{-1}$) under a HBSS environment for JDBM or WE43, which are currently considered candidates for Mg-based biodegradable alloys [43–46].

Detailed surficial conditions of the alloys immediately after immersion in HBSS for 12 h are provided in Fig. 6.

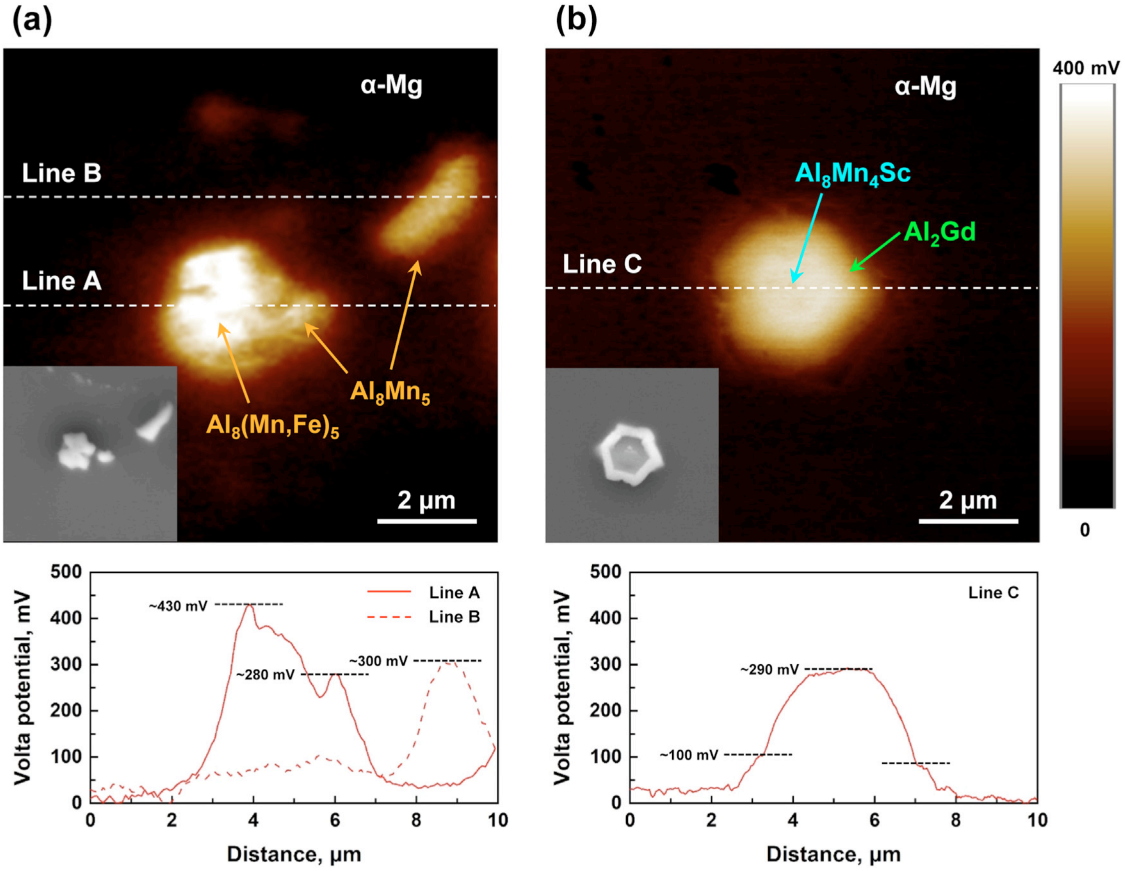

Fig. 4. SKPFM maps obtained from the (a) AZ31 and (b) AZ31-GS alloys with Volta potential profiles along the lines in the maps.

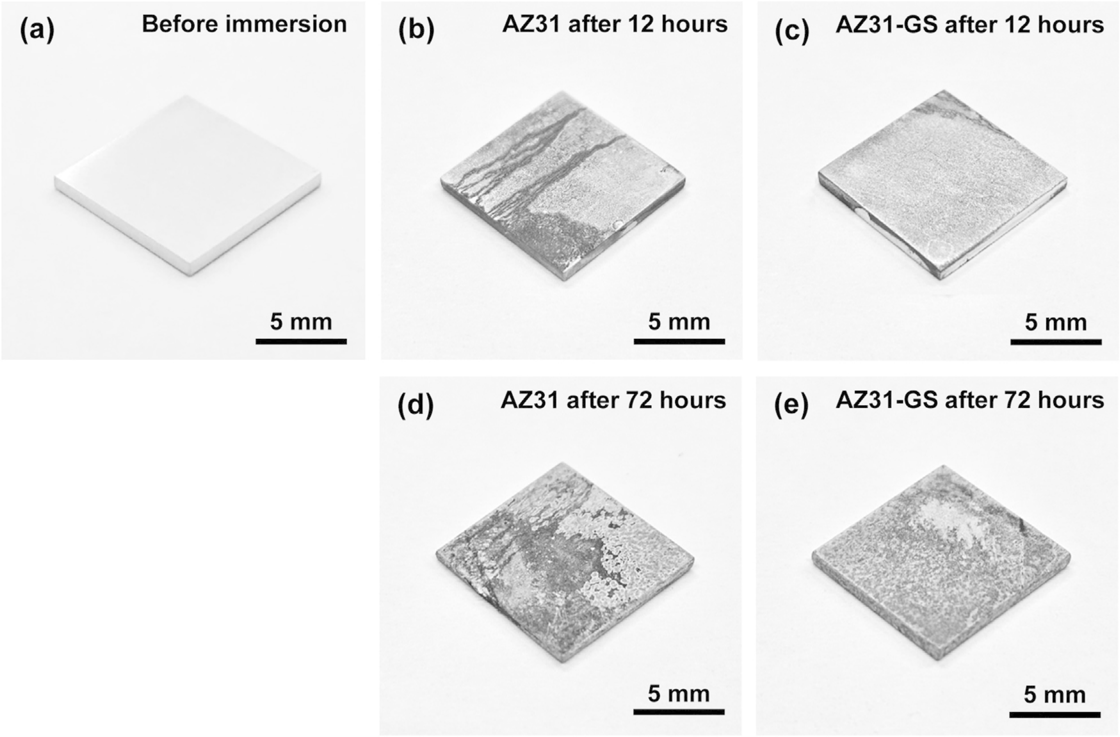

Fig. 5. Optical micrographs of the alloy samples in the hot-rolled condition before and after immersion in HBSS at 37 °C for 12 ∼ 72 h; (a) alloy before immersion, the (b) AZ31 and (c) AZ31-GS alloys after immersion for 12 h, and the (d) AZ31 and (e) AZ31-GS alloys after immersion for 72 h. The same scale bar applies to all subfigures.

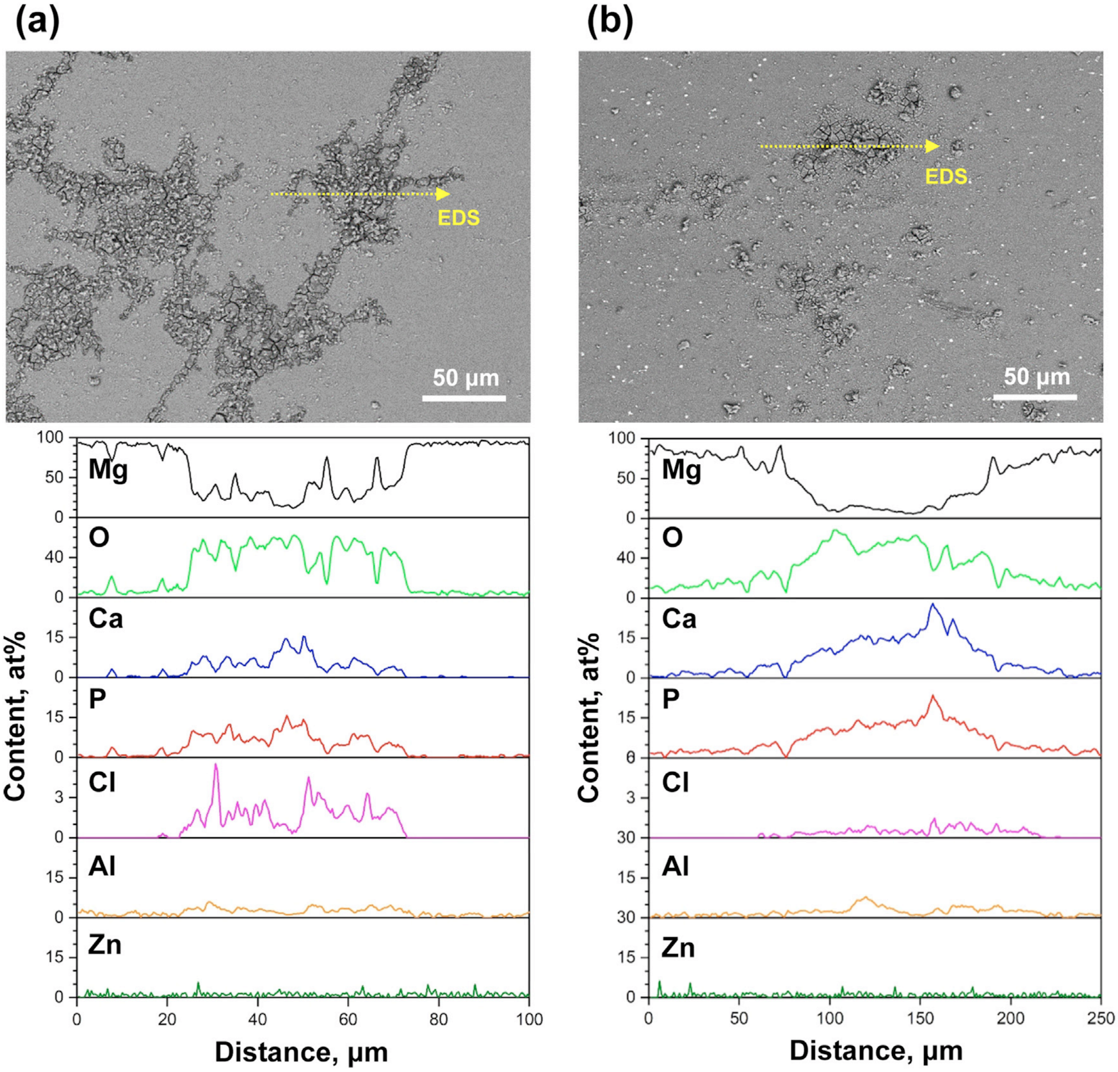

Fig. 6. SEM micrographs and EDS line profile results of the (a) AZ31 and (b) AZ31-GS alloys after immersion in HBSS at 37 °C for 12 h.

When comparing the overall surficial degradation products formed on the two alloys, the AZ31-GS alloy was found to be much less degraded than the AZ31 alloy after immersion. Degradation-induced scales formed on AZ31 appeared to be interlinked, similar to the corrosion patterns frequently observed in the commercial alloy immersed in an aqueous NaCl solution [39–41,47]. In contrast, the degraded parts of AZ31-GS were smaller and more isolated than those of AZ31, thus reinforcing that the former is more resistant to degradation in HBSS than the latter. An EDS analysis performed along the lines in the SEM micrographs indicated that elements of O, Ca, and P are mainly incorporated in the degradation products of both alloys and the contents of Ca and P along the lines vary almost equally in each alloy. This suggests that surficial scales containing both Ca and P are formed during immersion in HBSS. The AZ31-GS alloy presented higher Ca and P content and lower Cl content than the AZ31 alloy, which can be attributed to the relatively slow Mg degradation rate of the former [32]. From the EDS analysis, the atomic Ca/P ratios measured about 1.0 and 1.2 for the AZ31 and AZ31-GS alloys, respectively, indicating the latter has a higher Ca/P ratio. These differences in the surface oxide composition are a phenomenon often observed in Mg alloys that have different degradation resistance in HBSS [32]. Although hydroxyapatite, generally known as $Ca_{10}(PO_4)_6(OH)_2$, is one of the possible products in HBSS [48,49], the surface scale formed on the alloys may not be solely explained by its formation because its Ca/P ratio (1.67) is considerably higher than the Ca/P ratio values noted above. The conversion of $Mg(OH)_2$ to $Mg_3(PO_4)_2$ and $Ca_3(PO_4)_2$, as reported by Kalb et al. [50], or the formation of $Ca_2P_2O_7$ can be another plausible explanation for the surface scales formed on the AZ31 and AZ31-GS alloys. Although further analysis is needed, however, current XRD analysis suggests that the degradation products of the alloys are most likely composed of both hydroxyapatite and $Ca_2P_2O_7$, as shown in Fig. S1.

Fig. 7a–d present SEM micrographs and corresponding depth profiles of the AZ31 and AZ31-GS alloys after removing the surficial degradation products following immersion in HBSS for 12 h. As expected, the AZ31 alloy revealed

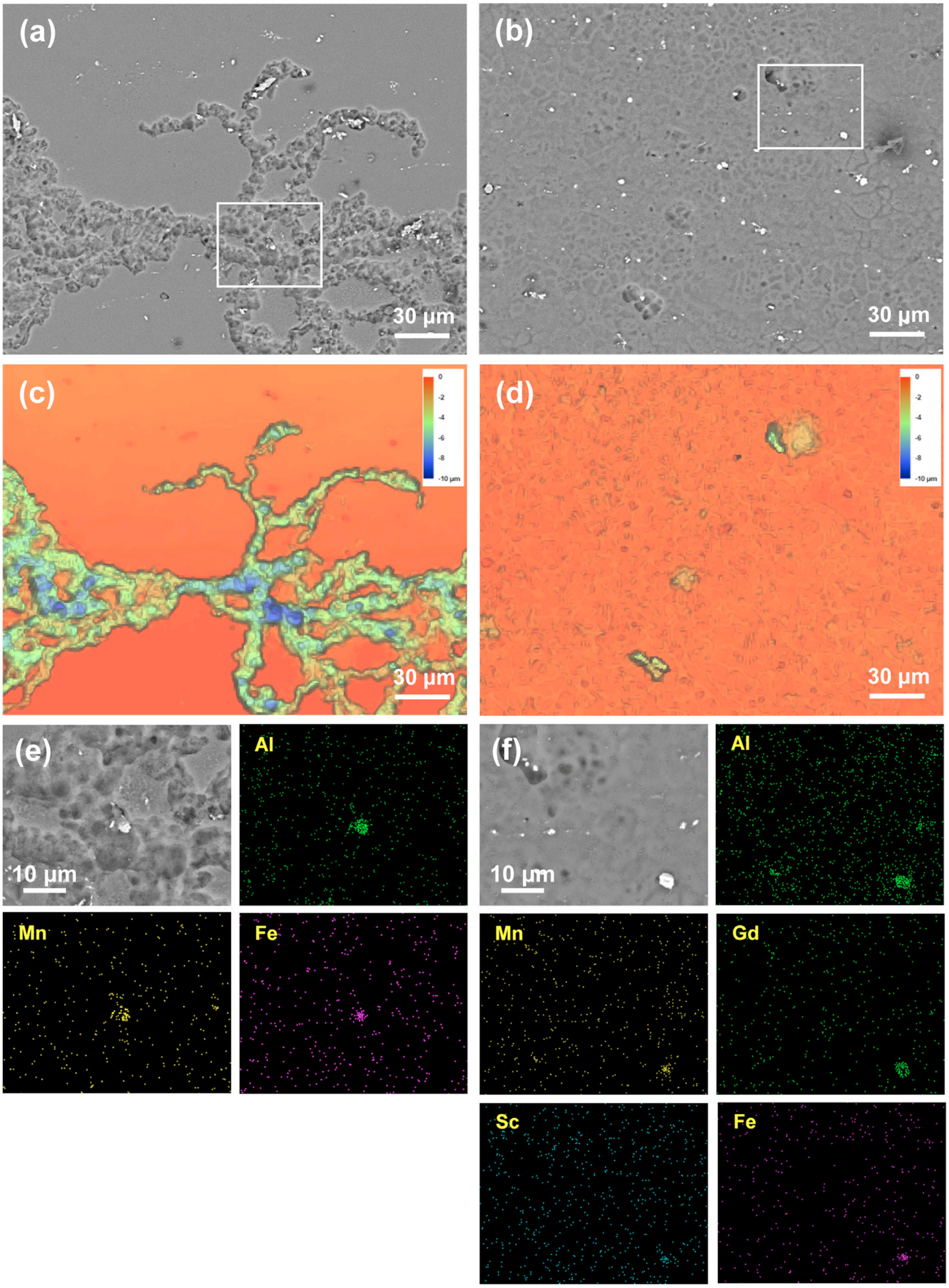

Fig. 7. (a and b) Low-magnification SEM micrographs and corresponding (c and d) depth profiles obtained after removing corrosion products from the (a and c) AZ31 and (b and d) AZ31-GS alloys immersed in HBSS at 37 °C for 12 h and magnified SEM micrographs of the rectangular regions of the (e) AZ31 and (f) AZ31-GS alloys with corresponding EDS maps for the elements Al, Mn, and Fe in AZ31 and Al, Mn, Gd, Sc, and Fe in AZ31-GS.

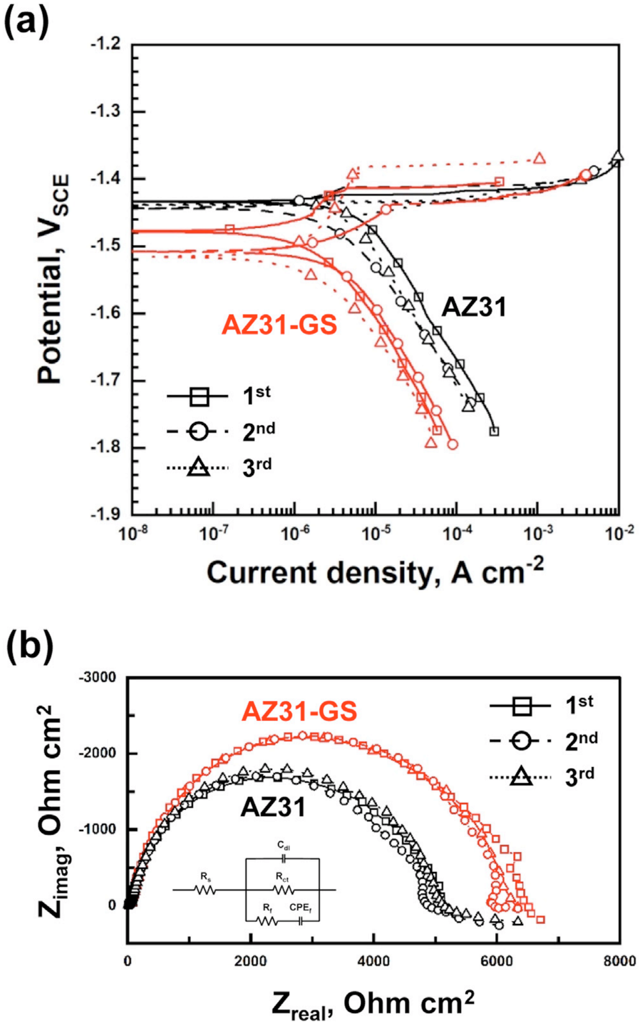

Fig. 8. (a) Potentiodynamic polarization curves and (b) Nyquist plots of the AZ31 and AZ31-GS alloys obtained after immersion in HBSS at 37 °C for one hour. The equivalent circuit for fitting is inset in (b).

extensive damaged areas with the maximum damage depth approaching ∼10 μm whereas the AZ31-GS alloy showed a relatively smooth surface with damage depths of less than ∼5 μm, relative to the nearly undamaged part. As shown in Fig. 7e, $Al_8Mn_5$ particles containing Fe can be seen in the deeply damaged parts of AZ31, suggesting they contribute to the occurrence of microgalvanic corrosion in HBSS. In contrast, the SEM micrograph in Fig. 7f indicated that microgalvanic corrosion is not as distinct in AZ31-GS, which does not have such Fe-rich particles in the microstructure.

### 3.4. Electrochemical analysis

Fig. 8a shows the potentiodynamic polarization curves of the AZ31 and AZ31-GS alloys after immersion in HBSS for one hour. The AZ31-GS alloy has a slightly lower corrosion potential than the AZ31 alloy; the average corrosion potentials are −1.437 and −1.501 $V_{SCE}$ for the AZ31 and AZ31-GS alloys, respectively. This decrease in corrosion potential has been frequently reported in Mg alloys with enhanced corrosion resistance and in many cases is mainly associated with a reduction in cathodic current density [40,51]. As for the anodic branch of the polarization curves, both alloys showed narrow passive potential ranges with considerable scattering, suggesting that they did not sufficiently retain the passivity of the surficial oxide film [25,49,52–54]. Unlike the alloy cases in this study, Mg alloys containing a large amount of RE have been known to have an appreciable passive potential range even under their bare alloy conditions [52,53]. With respect to the cathodic branch of the curves, the AZ31-GS alloy consistently showed lower cathodic current density than the AZ31 alloy in the investigated potential range. For instance, the current density values at −1.6 $V_{SCE}$ were 32.6 and 8.9 μA $cm^{-2}$ for the AZ31 and AZ31-GS alloys, respectively, indicating that the latter has about 3.5 times smaller cathodic current density than the former. This appreciable difference in the cathodic current density between the alloys is analogous to their dissimilar degradation rates observed during in vitro immersion testing.

To further study the electrochemical response of the alloys in HBSS, Nyquist plots were obtained from the EIS measurements. The Nyquist plots in Fig. 8b mostly show high-frequency capacitive loops regardless of the alloy types. The charge transfer resistance values obtained using the equivalent circuit for EIS data fitting were 5.1 and 6.5 kΩ $cm^2$ for the AZ31 and AZ31-GS alloys, respectively, indicating that they have marginally different EIS behaviors in the corrosive conditions. This is consistent with the above-mentioned results for the surficial degraded products, which show a slight difference in the Ca/P ratio between the two alloys.

### 3.5. In vivo degradation behavior

Fig. 9a show an optical micrograph taken during wire implantation in the femoral vein of a mouse. Successful wire implantation in this study was confirmed via CT imaging, as provided in Fig. 9b. The initial shape and surface condition of the wire immediately after implantation is presented through a 3D-reconstructed CT image in Fig. 9c. The tissues and degradation products surrounding the wire have relatively low X-ray permeability compared to the Mg alloys and are not expressed in this image. The surface morphologies of each alloy wire with various degradation periods can be seen in Fig. 9d–g. During implantation for up to 12 weeks, the AZ31 alloy wire showed an overall faster degradation rate than the AZ31-GS alloy wire. Although asperities and pitting were observed in both alloys, they were more pronounced in AZ31. The AZ31 alloy wire became significantly thinner after 12 weeks with non-uniform wire diameter at each site. In contrast, the AZ31-GS alloy wire showed a relatively gradual reduction of diameter without significant surface damage. After exposure to the biological environment for 12 weeks, only about 48 % and 75 % of the original volume remained for the AZ31 and AZ31-GS alloy wires, respectively, indicating that the latter is about twice as resistant to degradation in vivo as the former.

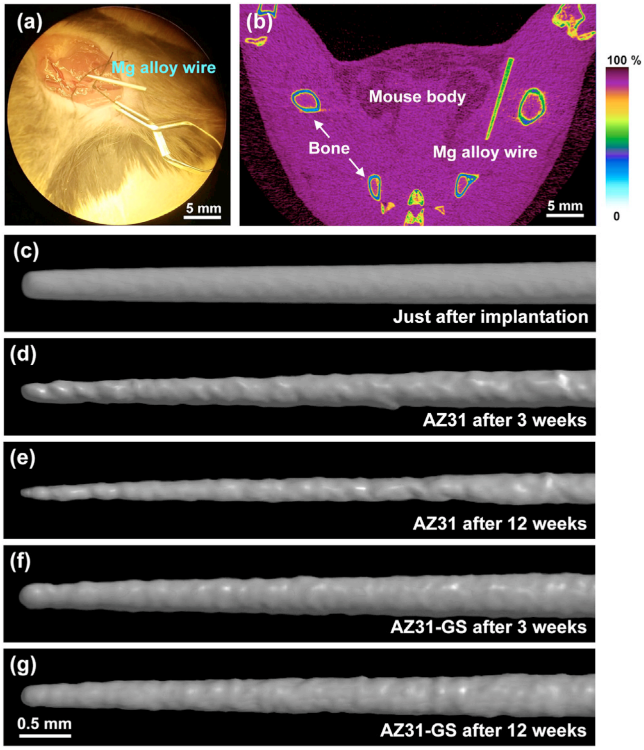

Fig. 9. (a) Optical micrograph showing the wire implantation procedure in this study, (b) a micro-CT image showing an implanted wire in a mouse, and 3D-reconstructed micro-CT images showing the alloy wires implanted in the femoral vein of a mouse for up to 12 weeks; (c) an as-implanted wire, the AZ31 alloy wires after implantation for (d) 3 and (e) 12 weeks, and the AZ31-GS alloy wires after implantation for (f) 3 and (g) 12 weeks.

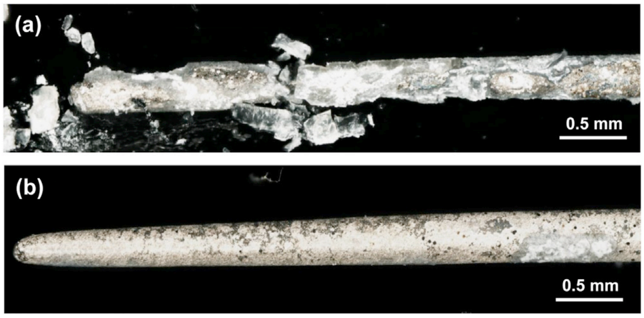

Fig. 10. Optical micrographs of the (a) AZ31 and (b) AZ31-GS alloy wires after implantation in the femoral vein of a mouse for 12 weeks.

Optical micrographs of the AZ31 and AZ31-GS alloy wires retrieved after implantation for 12 weeks are shown in Fig. 10. It can be seen that the surface of the AZ31 alloy wire is no longer smooth and some parts of the wire have already fragmented due to localized damage. In contrast, the AZ31-GS alloy wire mostly maintains its initial shape and metallic luster. This clearly shows that AZ31-GS has better resistance to in vivo degradation than AZ31, as similarly observed through in vitro degradation tests in HBSS. The detailed surface conditions of the alloy wires after implantation for 12 weeks can be seen in the SEM micrographs in Fig. 11. The AZ31-GS wire appears to be covered with non-metallic products on the surface while such protection against the degradation products is not as distinct on the surface of the AZ31 wire. This is suggestive of relatively active localized degradation in the case of AZ31 during the in vivo testing in the femoral vein of a mouse. The in vivo degradation rates were obtained based on the weight loss of the samples placed in the femoral vein for 12 weeks after removing the degradation products and were found to be 0.43 ± 0.07 and 0.20 ± 0.09 mm year$^{-1}$ for the AZ31 and AZ31-GS alloys, respectively. They revealed about twofold different degradation rates and both showed relatively lower rates compared to the in vitro environment evaluation.

### 3.6. Cell viability tests

The biocompatibility of the AZ31 and AZ31-GS alloys was evaluated by measuring the cytotoxicity of HUVECs treated with conditioned media prepared by incubating the AZ31 or AZ31-GS alloys in the cell culture media for three days. Fig. 12a shows fluorescent microscopic images of cells stained green remaining in the medium after exposure to each alloy's conditioned medium for one day. Dead cells stained red indicate cell metabolism activity has stopped. There was a remarkable decrease in the number of HUVECs with green fluorescence after being exposed to the AZ31 alloy conditioned media and the reduction of cell density was particularly severe. It appears that the ionic components extracted from the AZ31 alloy have a negative effect on the cell growth environment. In comparison, HUVECs exposed to AZ31-GS conditioned media show a homogeneous (similar level of) cell distribution as the control with a minor effect of observing some dead cells.

Another biocompatibility test based on the MTT analysis was conducted to quantitatively compare the biocompatibility of each alloy extract, as shown in Fig. 12b. The cell viability properties of each alloy extract were 69.3% ± 2.55% for AZ31 and 89.0% ± 5.87% for AZ31-GS, indicating that extract from AZ31-GS has a higher degree of cell viability than that from AZ31. It should be noted here that the cell viability result of the AZ31 alloy does not exceed the toxicity criteria suggested by the ISO-10993 cell viability test standard [55,56]. On the other hand, the AZ31-GS alloy, in which the extraction of Mg and other alloying elements was effectively inhibited, had only a slight negative effect on the activity of HUVEC, indicating that this alloy does not have significant toxicity to HUVECs in vitro. This is supported by the additional results in Fig. 12b showing that the cell viability of the AZ31-GS alloy in this study was similar to that of biodegradable WE43 and JDBM alloys available in the literature [56–58].

### 3.7. Factors affecting degradation and biocompatibility

This study shows that the corrosion-resistant AZ31-GS alloy containing novel second-phase particles with reduced electrochemical nobility provides much slower degradation behavior than the commercial AZ31 alloy in both in vitro and in vivo tests. Generally, corrosion of Mg-based materials in an

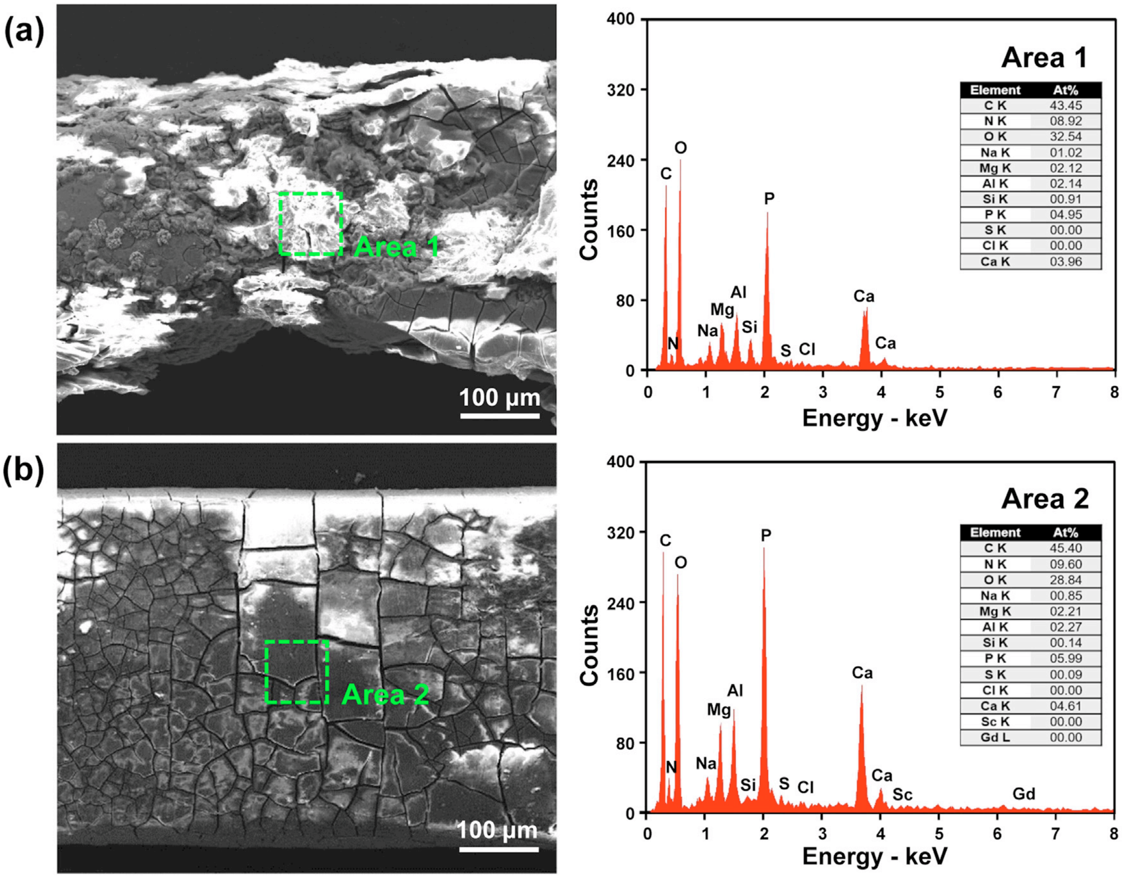

Area 1

| Element | At% |
|---|---|
| C K | 43.45 |
| N K | 08.92 |
| O K | 32.54 |
| Na K | 01.02 |
| Mg K | 02.12 |
| Al K | 02.14 |
| Si K | 00.91 |
| P K | 04.95 |
| S K | 00.00 |
| Cl K | 00.00 |
| Ca K | 03.96 |

Area 2

| Element | At% |
|---|---|
| C K | 45.40 |
| N K | 09.60 |
| O K | 28.84 |
| Na K | 00.85 |
| Mg K | 02.21 |
| Al K | 02.27 |
| Si K | 00.14 |
| P K | 05.99 |
| S K | 00.09 |
| Cl K | 00.00 |
| Ca K | 04.61 |
| Sc K | 00.00 |
| Gd L | 00.00 |

Fig. 11. SEM micrographs and EDS spectra of the (a) AZ31 and (b) AZ31-GS alloy wires implanted in the femoral vein of a mouse for 12 weeks.

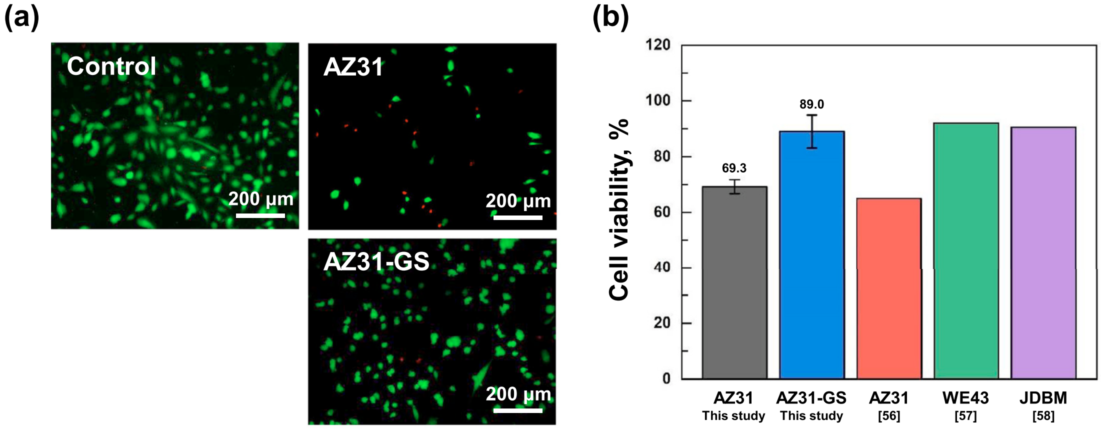

Fig. 12. (a) Fluorescent microscopic images of live (green) and dead (red) HUVECs after culture for 24 h in a medium conditioned with the AZ31 or AZ31-GS alloy with an unconditioned medium denoted as a control. (b) Cell viability results from MTT analysis for the Mg alloys in this study and other biodegradable Mg alloys available in the literature.

aqueous saline solution is greatly affected by $Cl^-$ ions, which readily penetrate surface oxide layers [59–63]. Since $Cl^-$ ions are available in HBSS in vitro as well as in blood in vivo, their role in decomposing the alloy materials is considered to be similarly influential and thus should not be overlooked in terms of degradation behavior [64]. Mg alloys with excellent corrosion resistance thus could be candidates for delayed degradation properties. In addition to the overall enhancement of degradation resistance, the in vivo test results in the mouse femoral vein clearly demonstrated that the degradation behavior of AZ31-GS was much more uniform than that of AZ31 in the biological environment. If the former is employed to fabricate a vascular stent, for instance, such sluggish and uniform degradation behavior would extend its functional maintenance period since locally damaged parts in the stent due to non-uniform degradation would not provide an initial dilatation force to the blood vessel [24,35].

This difference in the degradation behavior between the two Mg alloys investigated here can be understood from their electrochemical properties. The potentiodynamic polarization curves of the alloys in HBSS revealed that there is not a remarkable difference in the anodic branch of the polarization curves. This suggests an anodic reaction is not a decisive factor affecting the aforementioned difference in their degradation behavior. However, in the cathodic branch of the polarization curves, a clearly detectable difference between the alloys can be found. Retardation of the cathodic reaction thus may be the underlying mechanism mainly responsible for the slower and more uniform degradation behavior of the AZ31-GS alloy, as compared to the AZ31 alloy. This can be interpreted as a reduction of the cathodic $H_2$ evolution rate by microalloying with Gd and Sc, which leads to both microstructural and electrochemical changes that reduce the rate of microgalvanic corrosion between the $\alpha$-Mg matrix and nearby secondary intermetallic particles in the simulated physiological environment [28,40].

As shown in the cell viability tests, the AZ31-GS alloy yielded better results in the evaluation of cell formation and metabolic activity than the AZ31 alloy. Possible changes in ionic strength and pH associated with the decomposition by-products from the alloys increase the osmotic imbalance between the intracellular and extracellular environments and this osmotic shock can cause significant disruption of cellular metabolism, even resulting in apoptosis [65,66]. Therefore, it is important to minimize the amount of decomposition by-products of Mg alloys under the aqueous physiological environment to maintain biocompatibility. As indicated in the polarization curves and EIS results, the AZ31-GS alloy shows a lower degree of Mg dissolution and OH- generation compared to the AZ31 alloy. This can result in better biocompatibility when used as a biomaterial, similar to the previously mentioned effects of extractant exposure on HUVEC homeostasis. Despite the relative superiority of AZ31-GS, it is also desirable to conduct monitoring studies on the long-term biological effects of Gd and Sc, which contribute to reducing decomposition by-products.

## 4. Conclusion

The microstructure and the degradation behavior of an experimental corrosion-resistant AZ31-GS Mg alloy have been investigated and compared with those of a commercial AZ31 Mg alloy having a similar chemical composition. Novel core-shell particles were observed in AZ31-GS while typical Al-Mn particles with different levels of Fe content were found in AZ31. In vitro degradation rates obtained after 72 h-immersion in HBSS were 0.40 and 1.09 mm year$^{-1}$ for the AZ31-GS and AZ31 alloys, respectively. In vivo tests in the femoral vein of a mouse indicated that the AZ31-GS alloy degrades more slowly and uniformly than the AZ31 alloy. Microstructural and electrochemical analyses suggested that the unique degradation behavior of AZ31-GS is a result of retardation of the cathodic reaction in the biological corrosive conditions, which is originally associated with the presence of second-phase particles with reduced electrochemical nobility. Compared with WE43 and JDBM, which have been actively studied as Mg-based biodegradable alloys, the experimental AZ31-GS alloy in this study showed better degradation resistance with a similar level of cell viability, satisfying the basic requirements for use in Mg-based biodegradable implants.

## Declaration of competing interest

There is no actual or potential conflict of interest that can impact or be perceived to inappropriately impact on or influence the authenticity and/or reliability of the research contained in the manuscript. Prof. Sung Soo Park is an editorial board member for Journal of Magnesium and Alloys and was not involved in the editorial review or the decision to publish this article. All authors declare that there are no competing interests.

## CRediT authorship contribution statement

**Du-Won Min:** Writing – original draft, Investigation, Formal analysis. **Young Hee Kim:** Investigation. **Jaeho Kwon:** Investigation. **Jeong-Ki Kim:** Investigation. **Cholong Choi:** Methodology, Investigation. **Eunhye Yun:** Investigation. **Chaenyung Cha:** Supervision. **Seong Hoon Choi:** Methodology. **Hojong Park:** Methodology. **Jung Gu Lee:** Supervision. **Byungsuk Kwon:** Supervision. **Sang Jun Park:** Writing – original draft, Supervision, Methodology. **Sung Soo Park:** Writing – review & editing, Writing – original draft, Supervision, Funding acquisition, Conceptualization.

## Acknowledgments

This work was supported by the National Research Foundation of Korea (NRF) grant funded by the Korean government (MSIT) (No. RS-2023-00208762), the Ulsan University Hospital Research Grant (UUH-2020-01), and the 2025 Research Fund (1.250008.01) of UNIST (Ulsan National Institute of Science and Technology).

## Supplementary materials

Supplementary material associated with this article can be found, in the online version, at doi:10.1016/j.jma.2025.07.007.

Fig. S1. XRD patterns of the AZ31 and AZ31-GS alloys after immersion in HBSS for 12 h.

## References

[1] L. Mao, L. Shen, J. Chen, X. Zhang, M. Kwak, Y. Wu, R. Fan, L. Zhang, J. Pei, G. Yuan, C. Song, J. Ge, W. Ding, Sci. Rep. 7 (2017) 46343.
[2] M.P. Staiger, A.M. Pietak, J. Huadmai, G. Dias, Biomater 27 (2006) 1728–1734.

[3] K. Kapnisis, G. Constantinides, H. Georgiou, D. Cristea, C. Gabor, D. Munteanu, B. Brott, P. Anderson, J. Lemons, A. Anayiotos, J. Mech. Behav. Biomed. Mater. 40 (2014) 240–251.

[4] N. Sezer, Z. Evis, S.M. Kayhan, A. Tahmasebifar, M. Koç, J. Magnes. Alloys 6 (2018) 23–43.

[5] M. Moravej, D. Mantovani, Int. J. Mol. Sci. 12 (2011) 4250–4270.

[6] D.A. Pule, W.W. Huh, J. Appl. Biomater. 6 (1995) 109–116.

[7] C. Lhotka, T. Szekeres, J. Orthop. Res. 21 (2003) 189–195.

[8] Y. Niki, H. Matsumoto, Y. Suda, T. Otani, K. Fujikawa, Y. Toyama, N. Hisamori, A. Nozue, Biomater 24 (2003) 1447–1457.

[9] J.Y. Wang, B.H. Wicklund, R.B. Gustilo, D.T. Tsukayama, Biomater 17 (1996) 2233–2240.

[10] J.M. Anderson, A. Rodriguez, D.T. Chang, Semin. Immunol. 20 (2008) 86–100.

[11] V.V. Ramalingam, P. Ramasamy, M.D. Kovukkal, G. Mylisamy, Met. Mater. Int. 26 (2020) 409–430.

[12] H. Yan, X. Gong, J. Chen, M. Cheng, Met. Mater. Int. 26 (2021) 2249–2263.

[13] S.M. Mousavizadeh, S.H. Tabaian, Met. Mater. Int. 27 (2021) 5074–5081.

[14] P. Erne, M. Schier, T.J. Resink, Cardiovasc. Intervent. Radiol. 29 (2006) 11–16.

[15] H. Dong, F. Lin, A.R. Boccaccini, S. Virtanen, Corros. Sci. 182 (2021) 109278.

[16] P.K. Bowen, J. Drelich, J. Goldman, Adv. Mater. 25 (2013) 2577–2582.

[17] H. Yang, B. Jia, Z. Zhang, X. Qu, G. Li, W. Lin, D. Zhu, K. Dai, Y. Zheng, Nat. Commun. 11 (2020) 401.

[18] D. Bairagi, S. Mandal, J. Magnes. Alloys 10 (2022) 627–669.

[19] M. Haghshenas, J. Magnes. Alloys 5 (2017) 189–201.

[20] U. Riaz, I. Shabib, W. Haider, J. Biomed. Mater. Res. B: Appl. Biomater. 107 (2019) 1970–1996.

[21] A. Kumar, A. Choudhari, A.K. Gupta, A. Kumar, J. Magnes. Alloys 12 (2024) 3841–3897.

[22] G. Kumar, S. Preetam, A. Pandey, N. Birbilis, S. Al-Saadi, P. Pasbakhsh, M. Zheludkevich, P. Balan, J. Magnes. Alloys 13 (2025) 948–981.

[23] J. Espiritu, M. Meier, J.M. Seitz, Bioact. Mater. 6 (2021) 4360–4367.

[24] J.A. Grogan, B.J. O'Brien, S.B. Leen, P.E. McHugh, Acta Biomater 7 (2011) 3523–3533.

[25] Z. Gui, Z. Kang, Y. Li, Mater. Sci. Eng. C 96 (2019) 831–840.

[26] M. Esmaily, J.E. Svensson, S. Fajardo, N. Birbilis, G.S. Frankel, S. Virtanen, R. Arrabal, S. Thomas, L.G. Johansson, Prog. Mater. Sci. 89 (2017) 92–193.

[27] A. Atrens, G.-L. Song, M. Liu, Z. Shi, F. Cao, M.S. Dargusch, Adv. Eng. Mater. 17 (2015) 400–453.

[28] G.-L. Song, A. Atrens, Adv. Eng. Mater. 5 (2003) 837–858.

[29] F. Witte, N. Hort, C. Vogt, S. Cohen, K.U. Kainer, R. Willumeit, F. Feyerabend, Curr. Opin. Solid State Mater. Sci. 12 (2008) 63–72.

[30] J. Kuhlmann, I. Bartsch, E. Willbold, S. Schuchardt, O. Holz, N. Hort, D. Hoche, W.R. Heineman, F. Witte, Acta Biomater 9 (2013) 8714–8721.

[31] M.R. Sahu, T.S.S. Kumar, U. Chakkingal, J. Magnes. Alloys 10 (2022) 2094–2117.

[32] Y. Song, D. Shan, R. Chen, F. Zhang, E.-H Han, Mater. Sci. Eng. C 29 (2009) 1039–1045.

[33] R. Waksman, R. Erbel, C.D. Mario, J. Bartunek, B.D. Bruyne, F.R. Eberli, P. Erne, M. Haude, M. Horrigan, C. Ilsley, D. Böse, H. Bonnier, J. Koolen, T.F. Lüscher, N.J. Weissman, JACC Cardiovasc. Interv. 2 (2009) 312–320.

[34] Y. Shi, L. Zhang, J. Chen, J. Zhang, F. Yuan, L. Shen, C. Chen, J. Pei, Z. Li, J. Tan, G. Yuan, Mater. Sci. Eng. C 80 (2017) 1–6.

[35] J. Ma, N. Zhao, L. Betts, D. Zhu, J. Mater. Sci. Technol. 32 (2016) 815–826.

[36] J. Zhang, H. Li, W. Wang, H. Huang, J. Pei, H. Qu, G. Yuan, Y. Li, Acta Biomater 69 (2018) 372–384.

[37] G. Adegoke, et al., Evaluation of certain food additives and contaminants, Sixty-seventh report of the Joint FAO/WHO Expert Committee on Food Additives, World Health Organization, 2007, pp. 33–44. (WHO Technical Report Series, No. 940).

[38] Y. Liu, S. Zheng, N. Li, H. Guo, Y. Zheng, J. Peng, Sci. Rep. 7 (2017) 40184.

[39] G. Williams, H.L. Dafydd, R. Grace, Electrochim. Acta 109 (2013) 489–501.

[40] G.-L. Song, Z. Xu, Electrochim. Acta 55 (2010) 4148–4161.

[41] A. Samaniego, I. Llorente, S. Feliú Jr., Corros. Sci. 68 (2013) 66–71.

[42] M.F. Hurley, C.M. Efaw, P.H. Davis, J.R. Croteau, E. Graugnard, N. Birbilis, Corros. 71 (2015) 160–170.

[43] Y. Zong, G. Yuan, X. Zhang, L. Mao, J. Niu, W. Ding, Mater. Sci. Eng. B 177 (2012) 395–401.

[44] N. Li, C. Guo, Y.H. Wu, Y.F. Zheng, L.Q. Ruan, Corros. Eng. Sci. Technol. 47 (2012) 346–351.

[45] E. Galvin, S. Jaiswal, C. Lally, B. MacDonald, B. Duffy, J. Manuf. Mater. Process. 1 (2017) 8.

[46] X.B. Zhang, G.Y. Yuan, Z.Z. Wang, Mater. Sci. Technol. 29 (2013) 111–116.

[47] S.-M. Baek, S.-Y. Lee, J.C. Kim, J. Kwon, H. Jung, S. Lee, K.-S. Lee, S.S. Park, Corros. Sci. 178 (2021) 108998.

[48] M. Bornapour, N. Muja, D. Shum-Tim, M. Cerruti, P. Pekguleryuz, Acta Biomater 9 (2013) 5319–5330.

[49] B. Yavuzyegit, A. Karali, A.D. Mori, N. Smith, S. Usov, P. Shashkov, R. Bonithon, G. Blunn, ACS Appl. Bio Mater. 7 (2024) 1735–1747.

[50] H. Kalb, A. Rzany, B. Hensel, Corros. Sci. 57 (2012) 122–130.

[51] W. Wu, Z. Wang, S. Zang, X. Yu, H. Yang, S. Chang, ACS Omega 5 (2020) 941–947.

[52] P.-W. Chu, C.-W. Fan, C.-H. Yang, Mater. Chem. Phys. 312 (2024) 128609.

[53] L. Jiang, F. Xu, Z. Xu, Y. Chen, X. Zhou, G. Wei, H. Ge, Int. J. Electrochem. Sci. 10 (2015) 10422–10432.

[54] M.S. Uddin, C. Hall, P. Murphy, Sci. Technol. Adv. Mater. 16 (2015) 053501.

[55] J. Wang, F. Witte, T. Xi, Y. Zheng, K. Yang, Y. Yang, D. Zhao, J. Meng, Y. Li, K. Chan, L. Qin, Acta Biomater 21 (2015) 237–249.

[56] J. Wu, D. Zhao, B. Lee, A. Roy, R. Yao, S. Chen, Z. Dong, W.R. Heineman, P.M. Kumta, ACS Biomater. Sci. Eng. 6 (2020) 1950–1964.

[57] L. Mao, L. Shen, J. Niu, J. Zhang, W. Ding, Y. Wu, R. Fan, G. Yuan, Nanoscale 5 (2013) 9517–9522.

[58] L. Mao, H. Zhou, L. Chen, J. Niu, L. Zhang, G. Yuan, C. Song, J. Alloys Compd. 720 (2017) 245–253.

[59] A. Atrens, G.-L. Song, F. Cao, Z. Shi, P.K. Bowen, J. Magnes. Alloys 1 (2013) 177–200.

[60] Y. Song, E.-H. Han, K. Dong, D. Shan, C.D. Yim, B.S. You, Corros. Sci. 72 (2013) 133–143.

[61] E. Ghali, Corros. Magnes. Alloys (2011) 66–114.

[62] S.-M. Baek, J.S. Kang, H.-J. Shin, C.D. Yim, B.S. You, H.-Y. Ha, S.S. Park, Corros. Sci. 118 (2017) 227–232.

[63] S.-M. Baek, J.-K Kim, D.-W. Min, S.S. Park, J. Magnes. Alloys 11 (2023) 991–997.

[64] L. Han, Z. Zhang, J. Dai, X. Li, J. Bai, Z. Huang, C. Guo, F. Xue, C. Chu, J. Magnes. Alloys 11 (2023) 1043–1056.

[65] C.D. Bortner, J.A. Cidlowski, Front. Cell Dev. Biol. 25 (2020) 611211.

[66] L. Galluzzi, T. Yamazaki, G. Kroemer, Nat. Rev. Mol. Cell Biol. 19 (2018) 731–745.